Polarimetrically augmented Coherent Change Detection three stage detector for laboratory multistatic Synthetic Aperture Radar

Alexander Hagelberg [1], Daniel Andre [1], Mark Finnis [2]

[1] Centre for Electronic Warfare, Information and Cyber, Cranfield University, Defence Academy of the United Kingdom, SN6 8LA, UK

[2] Centre for Defence Engineering, Cranfield University, SN6 8LA, Defence Academy of the United Kingdom, SN6 8LA, UK

1 Introduction

Synthetic Aperture Radar (SAR) is an image formation technique that uses a moving transmitter and/or receiver to form high resolution radar images [1]. Because SAR uses microwave frequency electromagnetic (EM) waves rather than visible light, and is an active sensor, it allows for reconnaissance and surveillance for all weather, during the day and night. SAR Coherent Change Detection (CCD) allows for the detection of very small scene changes between SAR images, such as vehicle tracks[2, 3]. However, high contrast CCD results are reliant on high coherence between the SAR images [1].

In a CCD image a change is detected as a '*decorrelation*' over corresponding SAR image patches. These decorrelations originate from several sources [1, 4–7]. One of these is natural processes such as wind and rain which lead to greater decorrelation for longer greater times between repeat passes. To reduce the decorrelation from natural processes such as wind and rain, and to monitor developing situations in a timely manner, it is desirable to rapidly conduct the required repeated pass SAR collections.

In a monostatic SAR system the transmitter and receiver are co-located. In a bistatic system they are separated by a significant distance. A multistatic system utilises multiple transmitters or receivers. Multistatic SAR has several advantages, such as providing improved cross range resolution [8, 9], and Signal to Noise Ratio (SNR) [10], although the choice of which trajectories to combine significantly affects these [11].

Multistatic constellations may allow change detection images to be formed using SAR image collections from a wide variety of different trajectories, thus potentially reducing the repeat pass time [12, 13], however these may be subject to varying degrees of interferometric baseline and therefore coherence. This data is multidimensional and can be combined in different ways. For high coherence and improved change detection capability, the repeat pass geometries should be chosen to provide a high degree of spatial frequency support overlap [1, 14, 15], yet it has been found that this alone is insufficient to guaranty high coherence and good CCD contrast.

Applications include the multistatic SAR constellation being developed by the UK MOD under the name Project Oberon [16]. Such constellations may be able to provide timely repeat pass imagery. This research can also be applied to drone SAR swarms currently under development, which are intended to operate in SAR near field multistatic configurations [17, 18].

Polarimetric SAR CCD has also been shown to improve CCD images [3, 19, 20]. A two-stage intensity and CCD change detector has been demonstrated in [21–23]. This paper combines polarimetric decompositions and scattering mechanisms with CCD images to investigate the improvement in detection performance using multistatic and multipolarimetric SAR data. The detector performance will be quantified using performance metrics (see section 3.3).

This research is supported by measurements at the Cranfield University Ground Based Synthetic Aperture Radar (GBSAR) laboratory, where the antennas are scanned within two vertical rectangular apertures, allowing for a great deal of flexibility and control of SAR geometries for the scene.

2 Background

2.1 Coherent Change Detection (CCD)

Forming good quality high contrast CCD results is reliant on high coherence between the SAR images [1, 20, 24]. This coherence can be reduced by natural processes such as wind and rain [4, 7, 24, 25]. Conducting rapid repeated passes would allow for monitoring developing situations in a timely manner and provide better coherence.

For high coherence and an improved change detection capability, the repeat pass geometries should be chosen to provide a high degree of spatial frequency (K-space) support overlap [1, 14, 15], yet it has been found that this alone is insufficient to guaranty high coherence and good CCD contrast [5].

Coherent Change Detection (CCD) is calculated as a normalised complex cross correlation [1, 4, 26]. The magnitude, $\hat{\boldsymbol{\gamma}}$, is referred to as the sample coherence. Where S_1 and S_2 are the two complex images being compared and N is the number of pixels within a window sampled over the two images.

$$\hat{\gamma} = \frac{\left|\sum_{k=1}^{N} S_1(k) S_2^*(k)\right|}{\sqrt{\sum_{k=1}^{N} |S_1(k)|^2 \sum_{k=1}^{N} |S_2(k)|^2}} \tag{1}$$

2.2 Multidimensional CCD and two Stage detectors

The multistatic SAR data is multidimensional and can be combined in different ways. In this case multistatic data consists of three bistatic collections and four polarisations. This data can be processed in a variety of ways [11, 20].

A two-stage detector was presented in [21, 23], with [22] performing analysis on the theoretical performance. These detectors are described as 'combined intensity and coherent change detection'. For the Non-Coherent Change Detection (NCCD), changes are detected due to a difference in amplitude in the images. This typically indicates large scale scene changes. Smaller scene changes typically do not result in a change in intensity, but rather phase [1]. To detect these small-scale changes CCD is used.

The two-stage detector, introduced in [21, 23], is shown below in Figure 2.1 (replicated from [21]). Here S_1 and S_2 represent the reference and mission trajectories.

For the Intensity change detection, the difference in intensities (σ) is calculated. This difference is then compared against a threshold T_{NCCD}. Differences exceeding this threshold are labelled as changes. The coherent change detection, as described in section 2.1 results in a coherence value, $\hat{\gamma}$. This value is also compared against a threshold T_{CCD}. In this case values exceeding the threshold (close to 1) are labelled as unchanged, whereas pixels with a value below the threshold are labelled as changes. The output of the detector is a binary value indicating a change or no change.

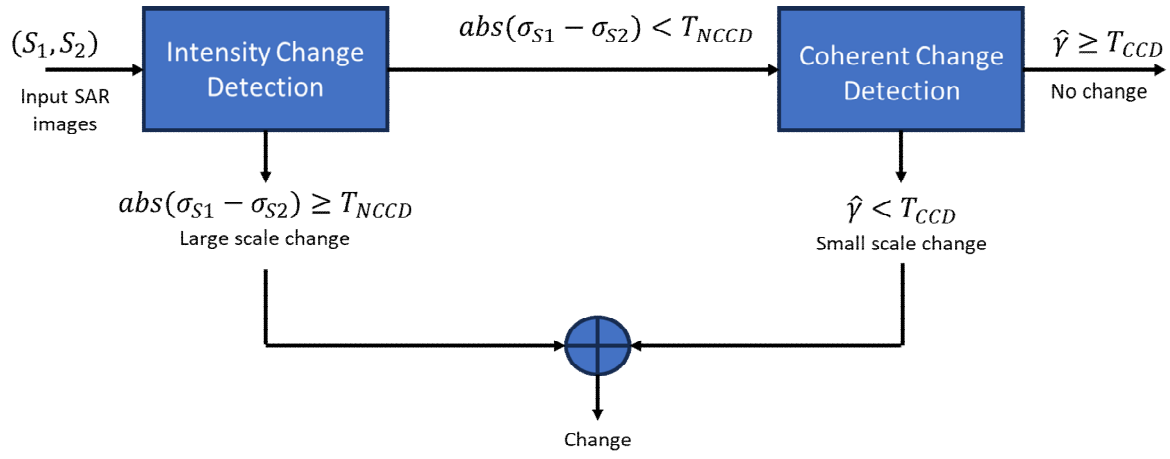

Figure 2.1 The block diagram of the two-stage detector introduced in [21, 23]. *Image is replicated from* [21]*, where it is figure 3. Image shows the Intensity and Coherent change detection stages as well as how thresholding is used.*

2.3 Polarimetry

Radar polarimetry uses the vector nature of electromagnetic waves to produce and analyse images. The main benefit of partial or fully polarimetric data collections is that the additional information provides a more detailed characterisation of the scatterer or target [3, 19, 26, 27], this is because the scattering of a target is dependent on the polarization and imaging geometry [28, 29]. Electromagnetic waves can be decomposed into vertical "V" or horizontal "H" polarisations. These are orthogonal to one and other.

These polarisations are used to describe the orientation of the EM waves as they are transmitted and received. VV means the antenna horns were set up to transmit and receive in the vertical polarisation. HH would mean the same but for the horizontal polarisation. VV and HH are referred to as the co-polar polarisations. There are also two cross-polar polarisations, VH and HV. In this case there is a mismatch between the transmit and receive polarisations. The nomenclature is to write received-transmitted. So a VH polarisation would be transmitted in horizontal and received in vertical.

Polarimetric decompositions are combinations of polarisations. Often these are used to characterise different scattering mechanisms [30].

The Scattering matrix, $\boldsymbol{S}$, is a 2x2 matrix. It describes the backscattering response and polarising properties of a target [31, 33]. This matrix is populated by complex variables called the complex scattering amplitude. The first column is for the scattering from horizontally transmitted waves, and the second for vertically transmitted waves. The Scattering matrix, $\boldsymbol{S}$ is defined as follows [26]:

$$\boldsymbol{S} = \begin{bmatrix} S_{hh} & S_{hv} \\ S_{vh} & S_{vv} \end{bmatrix} \tag{2}$$

It can be decomposed using the Pauli basis as follows:

$$\boldsymbol{S} = \begin{bmatrix} a+b & c-jd \\ c+jd & a-b \end{bmatrix} = a\begin{bmatrix} 1 & 0 \\ 0 & 1 \end{bmatrix} + b\begin{bmatrix} 1 & 0 \\ 0 & -1 \end{bmatrix} + c\begin{bmatrix} 0 & 1 \\ 1 & 0 \end{bmatrix} + d\begin{bmatrix} 0 & -j \\ j & 0 \end{bmatrix} \tag{3}$$

Here the factors a, b, c and d are all complex, and represent the contribution of canonical scattering mechanisms [26]. These can be determined from the scattering matrix.

- a, corresponds to the single (odd) bounce scattering from a plane or sphere.
- b, corresponds to double (even) bounce scattering from a dihedral.
- c, corresponds to double (even) bounce scattering from a dihedral, rotated 45 degrees with respect to the line of sight.
- d, corresponds to anti-symmetric helix type scattering. These transform the incident wave to its orthogonal polarisation state.

Rearranging (3) we get the formulas for a, b, c and d:

$$a = \frac{S_{hh} + S_{vv}}{2}; \quad b = \frac{S_{hh} - S_{vv}}{2}; \quad c = \frac{S_{hv} + S_{vh}}{2}; \quad d = \frac{S_{vh} - S_{hv}}{2j}; \tag{4}$$

A change in the value of the a, b, c or d variables is indicative of a change between the reference and mission trajectories. These polarimetric decompositions are used in the three-stage change detection process, see section 3.2.

3 Methodology

3.1 GBSAR laboratory

The GBSAR laboratory performs microwave measurements with a Vector Network Analyser (VNA), which generates a stepped frequency waveform. The system is currently set up for indoor use, with the VNA attached to two Ultra-Wideband horn antennas allowing measurements within the range 1-10 GHz. The two antenna horns are mounted on rails and are moved in two dimensional vertical apertures. These are shown in Figure 3.1. Because of the high positioning accuracy of the rail system, trajectories could be repeated and multistatic images formed.

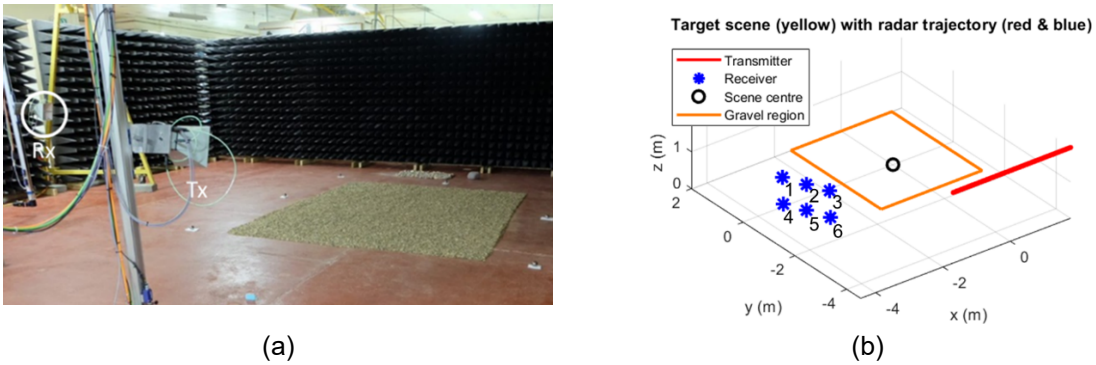

(a) (b)

Figure 3.1 Image (a) shows the GBSAR system in a bistatic configuration, with a gravel rectangle as the scene. Image (b) shows the radar trajectories used in the data collection. The transmitter trajectory is shown in red, the multiple fixed receiver positions in blue and the gravel region is shown in orange. The receivers are numbered 1 to 6 and are referred to as R1 through to R6.

In this experiment the 6.6-10 GHz band was used. A gravel rectangle, approximately 3.5 x 4 m, was located at the centre of the scene. This would provide speckled SAR images suitable for a coherence investigation and allow tracks to be drawn. The letters 'GBSAR' were traced on the gravel for use in change detection images.

3.2 Polarimetrically augmented three stage detector

A new three stage detector is proposed in this paper. Unlike previous examples it uses multistatic, fully polarimetric data.

"Maximum", "mean" and "minimum" are used to refer to the detections in the images, where the naming convention comes from CCD images: a maximum image has the maximum coherence value for each pixel between the different CCD images being compared (a maximum image results in the minimum number of detections). Conversely a minimum image has the lowest coherence (and the highest number of detections). This nomenclature is also used for the NCCD and polarimetric decomposition images.

However, in the NCCD and polarimetric decomposition images a higher value corresponds to a greater change. Therefore, to maximise the coherence or detections the following combinations were used for the two and three stage images:

- Max CCD – Min NCCD, Min Pol change
- Mean CCD – Mean NCCD, Mean Pol change
- Min CCD – Max NCCD, Max Pol change

3.2.1 Order of operations

The formation of the three-stage images is presented in this section. The processing has been broken down into three flow diagrams to aid in clarity.

The formation of a bistatic two-stage image is presented below in Figure 3.2. The multistatic case will be similar, albeit with additional images generated. First four sets of SAR images are compared using CCD and NCCD. This forms a CCD and NCCD image for each polarisation. For the multistatic case this would involve 12 sets of SAR images. The maximum, mean and minimum of the pixels in the CCD and NCCD images are then found.

This then allows for the two stage images to be formed. The two stage image is formed by applying a threshold to the CCD and NCCD images. T_{CCD} is applied to the CCD images and T_{NCCD} is applied to the NCCD images. The max two-stage image is named after the max CCD image maximises the coherence. This results in a lower number of detections, and the highest value for the two-stage image. The maximum CCD and minimum NCCD

images are used to form it. The mean two-stage is formed using the mean images. The minimum CCD image minimises the coherence and thus has the highest number of detections of change. As such, to form the minimum two-stage image the minimum CCD is used alongside the maximum NCCD.

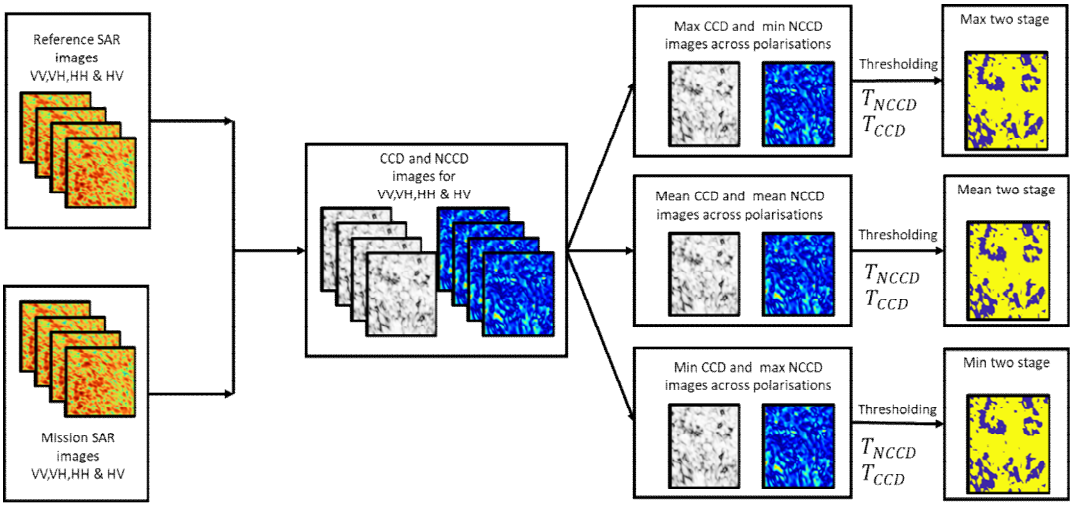

Figure 3.2 Flow diagram showing the formation of the two-stage change detection images.

The fully polarized SAR images are also used to form the polarimetric change images. This is shown in Figure 3.3. First the VV, VH, HH and HV images are decomposed into the a, b, c and d parameters (see equation (4)). The difference is then found between the reference and the mission images. This results in four images of the differences in polarimetric parameters. The maximum, mean and minimum of each pixel is then taken. For the multistatic case this would be done three times, resulting in 12 polarimetric change images that would then have the maximum, mean or minimum applied across them.

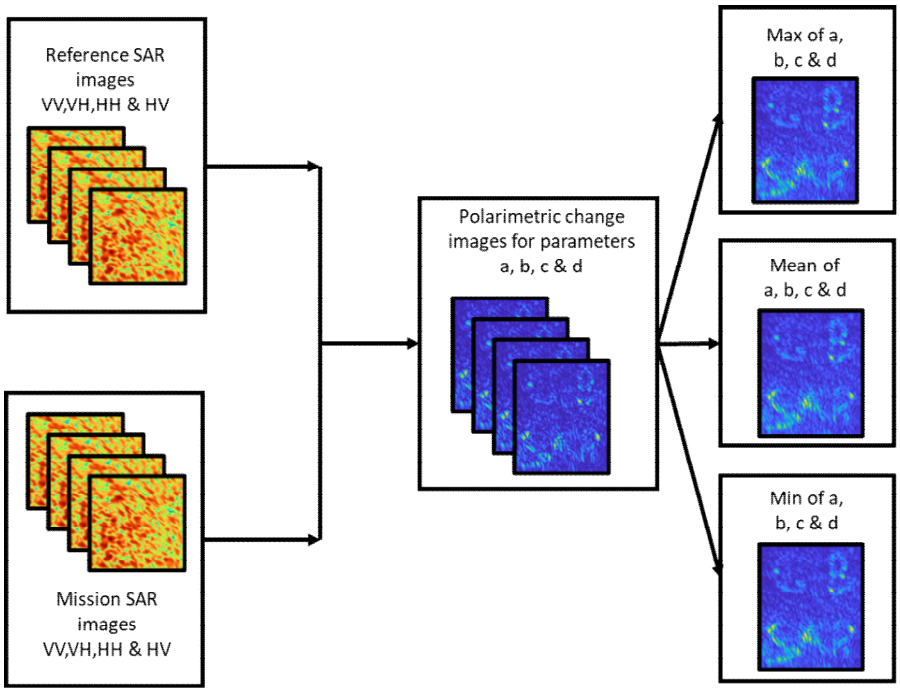

Figure 3.3 Flow diagram showing the formation of the polarimetric change images.

Finally the three-stage detector is presented. In this a threshold is applied to the two-stage detector images (Figure 3.2) and the polarimetric decomposition change images (Figure 3.3). The threshold $T_{2\,stage}$ is applied to the two-stage images and T_{pol} is applied to the polarimetric decomposition change images. The result is referred to as the three-stage image. This processing stage is the same for the bistatic or multistatic case as the two-stage and polarimetric change images are already either bistatic or multistatic.

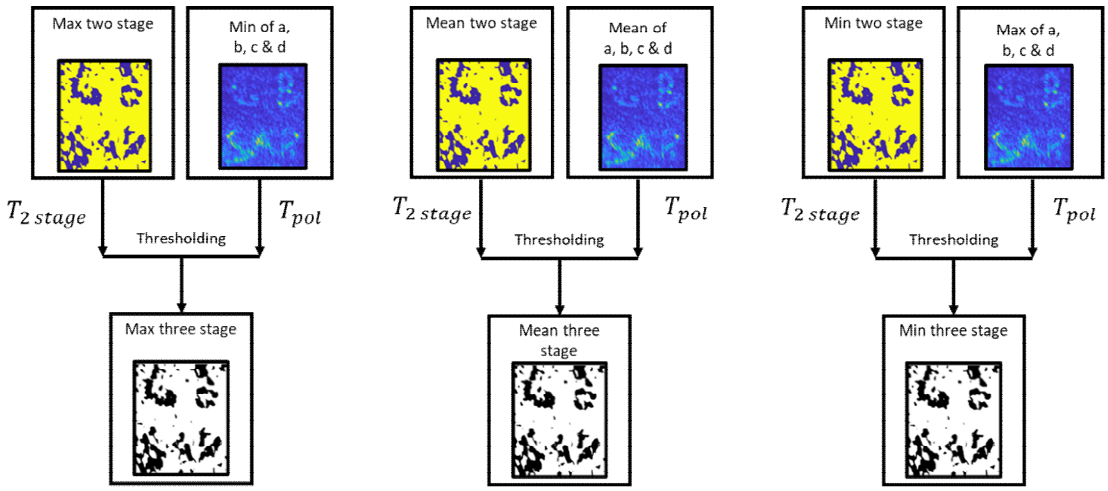

Figure 3.4 flow diagram showing the three-stage detector. It shows how the two-stage images and polarimetric decomposition change images are thresholded.

3.3 Data processing

The SAR images will be used to form CCD images. There were two sets of CCD images, one where the gravel was undisturbed, and another where the gravel had a disturbance track traced.

Performance metrics will be used in the evaluation of the CCD images. These metrics are often used in the evaluation of space weather predictive models [32, 34]. These are calculated using a confusion matrix. Here T and F mean true and false respectively, and P and N mean positive (change) and negative (no-change) in the CCD image [32, 35]. These are shown in a confusion matrix in Table 1.

Confusion Matrix		Event Observed	
		Yes	No
Event Forecast	Yes	TP	FP
	No	FN	TN

Table 1 Confusion matrix, showing the conditions that correspond to TP, TN, FP and FN.

Using the Confusion matrix several performance metrics can be calculated. The formulae for the metrics are shown in Table 2. Additional metrics such as the RMSE (to be defined below) use the coherence values of the images. These formulas are defined below [32, 34–39]:

- Probability of Detection (POD). This metric gives a value of [0,1] and is the proportion of true positive predictions compared to the number of events. A value approaching 1indicates most events were detected, and a value approaching 0 indicates most events were missed.
- The Critical Success index (CSI) shares some similarities with the POD. It compares the number of correct forecasts to the number of correct forecasts, false alarms and misses. It is not affected by the number of correct negative forecasts. A value approaching 1 indicates a perfect forecast.
- The False Alarm Rate (FAR) compares the number of false alarms with the number of forecast events. Here a value of 1 indicates all forecast events were false.
- The Proportion Correct (PC) provides a measure of the number of correct forecasts of events compared to the total number. A value approaching 1 indicates most forecasts were true, a value approaching 0 indicates most were wrong.
- The Heidke Skill Score (HSS) shares some similarities with the Success Rate (SR = 1 - FAR) , however it also accounts for the random forecasts. The HSS outputs a value of -∞ to 1. No incorrect forecasts would result in a value of +1. No correct forecasts would give a value of -∞. A value of 0 would indicate 'no skill', and performance close to random guesses.
- The Matthew's Correlation Coefficient (MCC) is an alternative to Pearson's Correlation Coefficient (R) but is less effected by unbalanced datasets. A value of 1 represents perfect classification, and -1 represents perfect miss-classification. Similarly to the HSS, a value of 0 represents a classification similar to the expected value (random or no skill).

- The root mean squared error (RMSE) is a measure of the difference in values rather than the forecasting of events. In this case 0 indicates no error, and any other positive value indicates an error.

Name	Formula	Value range	Eq. No.
Probability of Detection	$POD = \frac{TP}{TP + FN}$	[0,1]	(5)
Critical success Index	$CSI = \frac{TP}{TP + FP + FN}$	[0,1]	(6)
False Alarm Rate	$FAR = \frac{FP}{TP + FP}$	[0,1]	(7)
Proportion Correct	$PC = \frac{TP + TN}{TP + TN + FP + FN}$	[0,1]	(8)
Heidke Skill Score	$HSS = \frac{2 * (TP \cdot TN - FP \cdot FN)}{(TP + FN)(FT + TN) + (TP + FP)(FP + TN)}$	$[-\infty, 1]$	(9)
Matthews's Correlation Coefficient	$MCC = \frac{TP \cdot TN - FP \cdot FN}{\sqrt{(TP + FP) \cdot (TP + FN) \cdot (TN + FP) \cdot (TN + FN)}}$	$[-1,1]$	(10)
Root Mean Squared Error	$RMSE = \sqrt{\frac{1}{N}\sum_{i=1}^{N}(Predicted_i - Actual_i)^2}$	$[0, \infty]$	(11)

Table 2. Table shows the formulas and range of values for different performance metrics and skill scores.

Master CCD images will used to calculate the performance metrics. A master two stage image is shown in Figure 3.5 (a) with values ranging from -1 to 1. Figure 3.5 (b) shows a binary image where pixels with a coherence below a threshold were detected as a change and set to 0. Those with a coherence above the threshold were set to 1. This shows where detections of a change or no change would be made for the master image. The threshold for the master image was chosen as it most accurately replicated the ground truth of the disturbance. A lower threshold would have resulted in too large an area of detected changes, whereas a higher threshold would have resulted in parts of the letters being missed out.

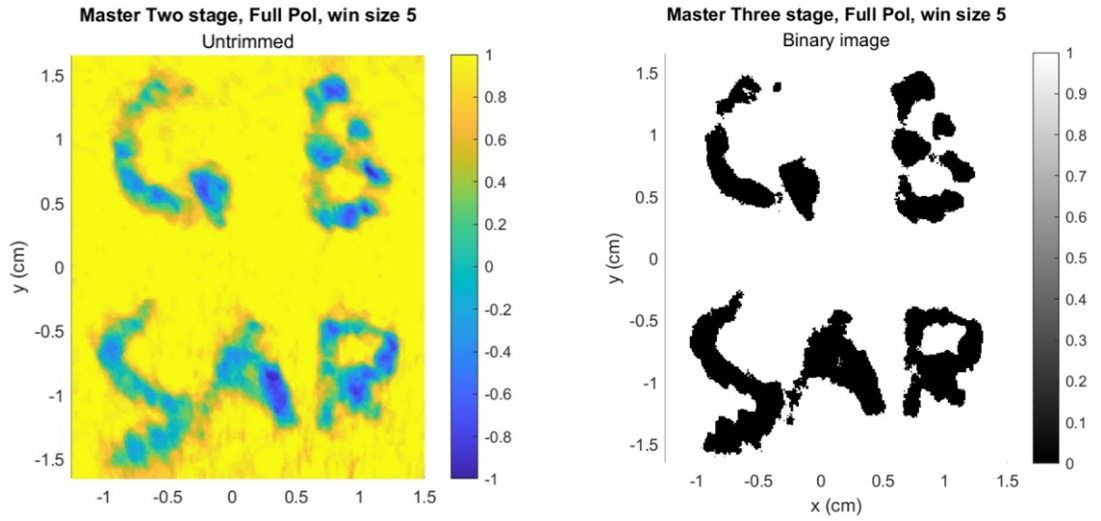

(a) (b)

Figure 3.5 Master images used for the performance metrics. Image (a) is a two-stage change image formed from fully polarized multistatic data collections. Image (b) is a three-stage change detection binary image formed from applying a threshold to (a) and the polarimetric decomposition change images.

4 Results

The performance of the three-stage change detection process can be plotted on s spider plot. This allows for the easy visualization of many separate variables. A higher value generally indicates good performance with the exception of FAR and RMSE, where high values indicate poor performance.

The performance of the bistatic images is plotted in Figure 4.1. Here it can be seen that the performance varies significantly depending on weather the bistatic image is formed from the maximum mean or minimum of the fully polarimetric data. It is also clear that using multiple variables is key to understanding the performance. Looking at the proportion correct and the RMSE the maximum and mean appear to perform very well. However, the POD shows that the maximum is missing a large number of the changes. The minimum images result in the best POD, and a decent PC, however, perform very poorly in all other metrics. Overall the mean images appear to perform the best for the bistatic case.

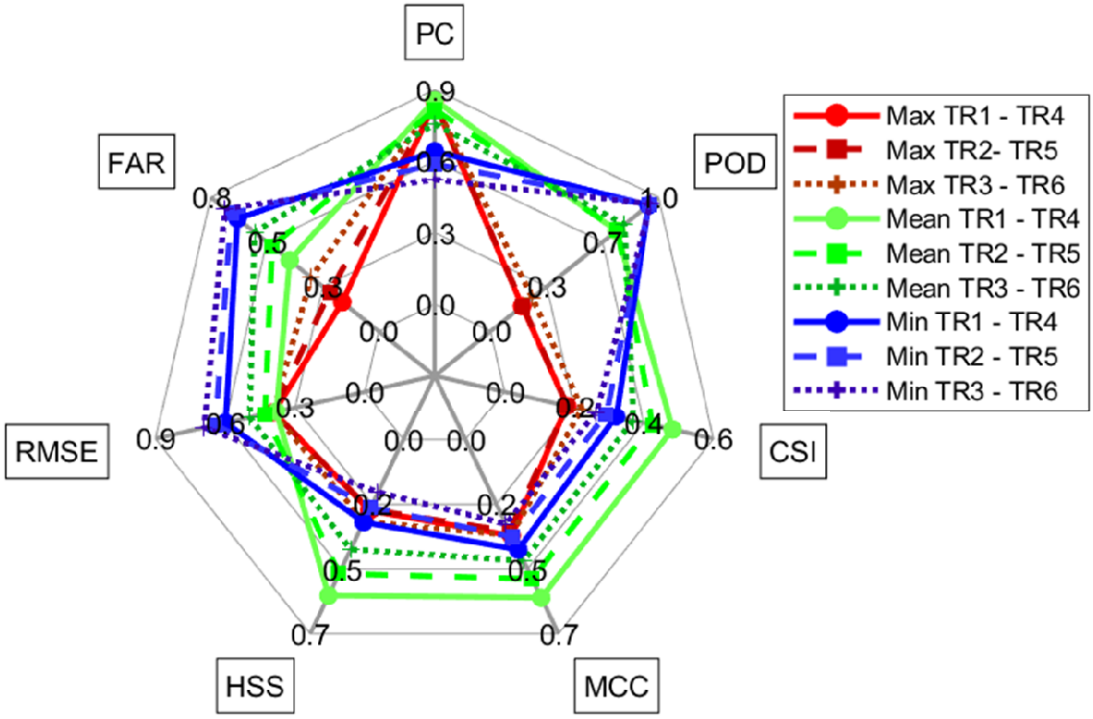

Figure 4.1 Spider plot of the three stage bistatic performance metrics. Maximum images are represented by red, mean by green and minimum by blue.

The trend shown in Figure 4.1 is repeated in

Figure 4.2. Here the mean images are clearly performing better than the maximum and minimum images. There are differences between the multistatic and bistatic performance metrics and these are shown in Figure 4.3, Figure 4.4 and Figure 4.5.

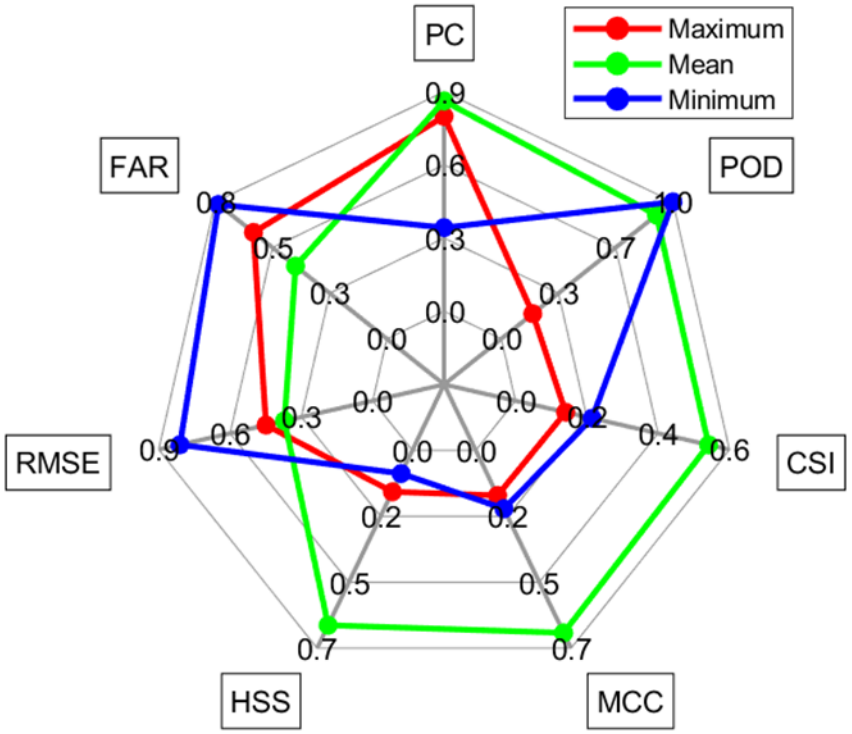

Figure 4.2 Spider plot of the three stage multistatic performance metrics. Maximum is represented by red, mean by green and minimum by blue.

In the case of the maximum (Figure 4.3) the performance of the HSS and PCC drop closer to zero indicating that the performance is approaching that of a random guess. The FAR however increases significantly from around 0.3 to 0.6.

The mean images (Figure 4.4) show an improvement in performance for all metrics. With a reduction in RMSE and FAR, and an increase in all other metrics.

The minimum images (Figure 4.5) show a drop in performance. In particular PC shows a significant drop from 0.6 to 0.3. Additionally, the HSS, CSI and MCC also show drops. The RMSE and FAR also increase. The POD does improve, however.

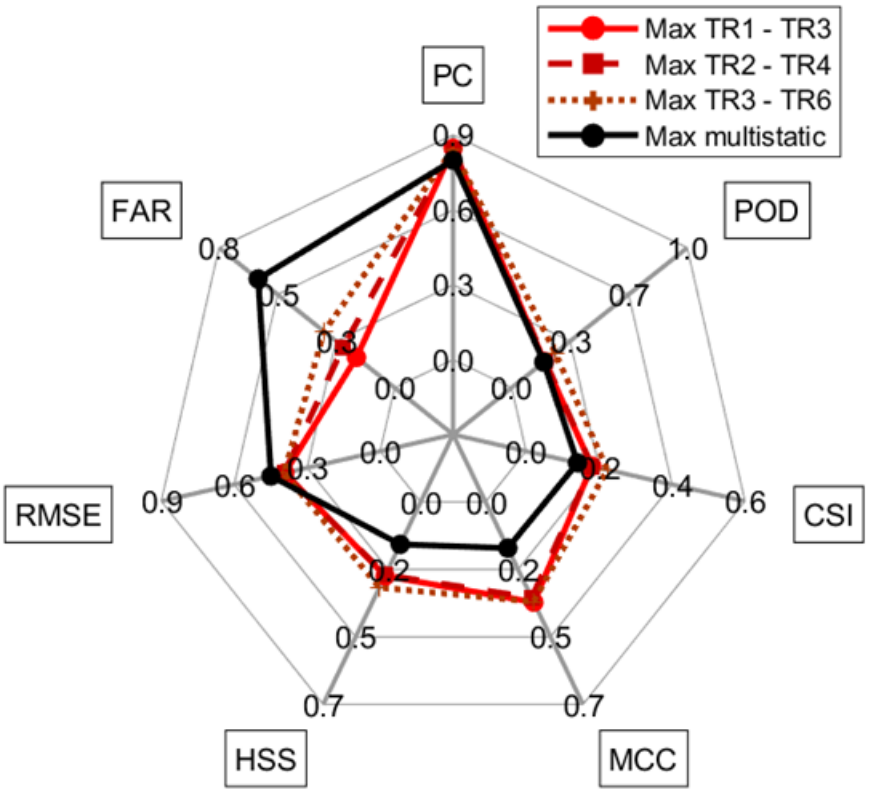

Figure 4.3 Spider plot showing the change in performance metrics between the three bistatic maximum images and the multistatic maximum image. The bistatic images are represented by red, and the multistatic image by black.

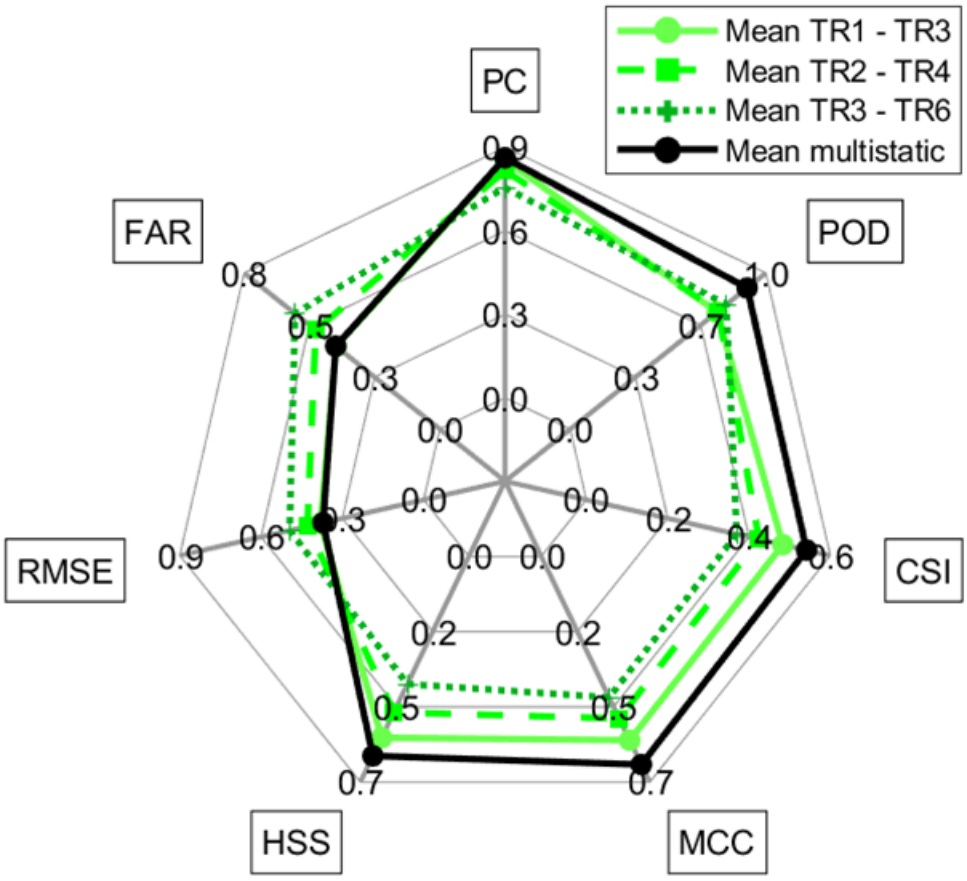

Figure 4.4 Spider plot showing the change in performance metrics between the three bistatic mean images and the multistatic mean image. The bistatic images are represented by green, and the multistatic image by black.

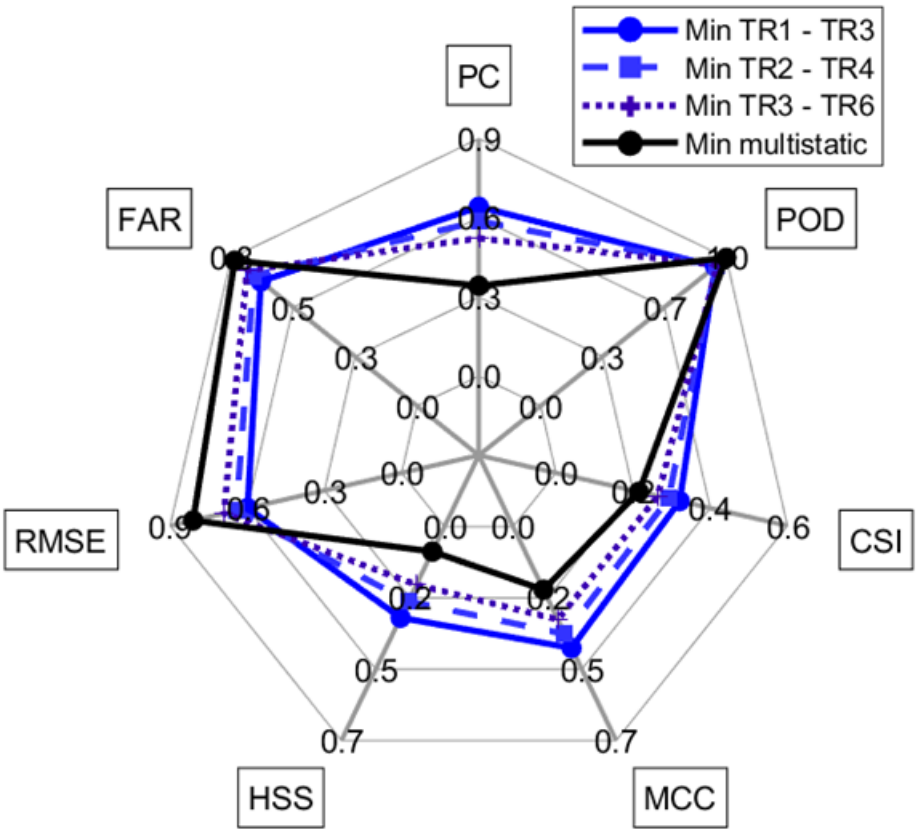

Figure 4.5 Spider plot showing the change in performance metrics between the three bistatic minimum images and the multistatic minimum image. The bistatic images are represented by blue, and the multistatic image by black.

The change in performance discussed above between the bistatic and multistatic collections can also be visualized using the 3 stage binary images. A tessellation of these is presented in Figure 4.6. Here white is a detection of no change and black a detection of a change. In the maximum images, the multistatic image contains significantly more detections of change than the bistatic images. This visualizes the drop in performance seen in Figure 4.3. The mean multistatic is visually more similar to the master (Figure 3.5), than the bistatic mean images. Finally, the minimum image appears quite similar to the bistatic minimum images, although it appears to have additional false detections. This aligns with the change in performance seen in figure Figure 4.5.

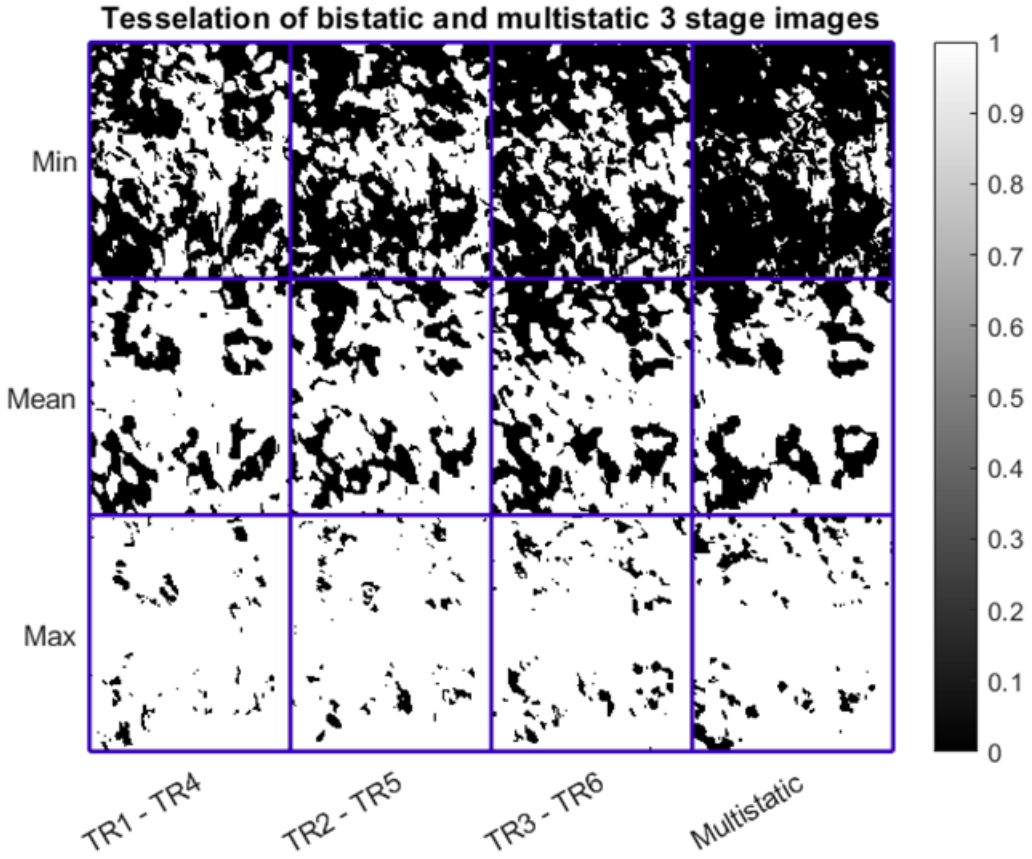

Figure 4.6 Tessellation of bistatic and multistatic three stage change images. The top row shows the minimum, the middle the mean and the bottom row the maximum. The minimum images have the most detections, and the 'GBSAR' becomes illegible for the multistatic. The maximum images have the fewest detections, and the 'GBSAR' remains unclear throughout. The minimum images show the 'GBSAR', although the multistatic bears greater resemblance to the master than the bistatic images.

5 Conclusion

In conclusion this paper has shown the feasibility of a three-stage change detector, using coherent and incoherent change detection data as well as polarimetric decompositions.

It has also investigated the performance of this change detector. It has been shown that simply relying on common performance metrics such as POD and FAR is insufficient to properly characterize the performance of a detector/forecast. Utilizing multiple performance metrics is advisable. Additionally inspecting the detector or model output (as was done for Figure 4.6) can also aid in the analysis of performance.

For this dataset, the mean multistatic performed best. This is a different result compared to [20], where the minimum appeared to perform best. It is believed that this is due to the change in the detector used. This suggests that attaining optimal detection is dependent on the processing used, and that attempting to maximize the detections in multistatic data does not always lead to the best results.

The polarimetric decomposition used was not roll-invariant, and future work could investigate the use of roll-invariant decompositions or parameters such as the Huynen fork.

6 References

1 Jakowatz, C. V., Wahl, D.E., Eichel, P.H., Ghiglia, D.C., Thompson, P.A.: 'Spotlight-mode synthetic aperture radar a signal processing approach' (Kluwer Academic Publishers, 1996)

2 Preiss, M., Gray, D.A., Stacy, N.J.S.: 'Detecting scene changes using synthetic aperture radar interferometry'*IEEE Transactions on Geoscience and Remote Sensing*, 2006, **44**, (8), pp. 2041–2054.

3 Preiss, M., Stacy, N.J.S.: 'Polarimetric SAR Coherent Change Detection' (2008)

4 Preiss, M., Stacy, J.: 'Coherent Change Detection: Theoretical Description and Experimental Results'*Defence Science and Technology Organisation (DSTO), Report no. DSTO–TR–1851*, 2006.

5 Hagelberg, A., Andre, D., Finnis, M.: 'Laboratory bistatic synthetic aperture radar coherent change detection investigation'*Electronics Letters (IET)*, 2023, **59**, (15), p. e12913.

6 Zebker, H.A., Member, S., Villasenor, J.: 'Decorrelation in Interferometric Radar Echoes'*IEEE Transactions on Geoscience and Remote Sensing*, 1992, **30**, (5).

7 Bickel, D.L.: 'SAR Image Effects on Coherence and Coherence Estimation'*Sandia National Laboratories, Report no. SAND2014-0369*, 2014.

8 Chung, C., Kim, S., Kim, J., Lee, U., Lee, B., Ka, M.H.: 'Analysis on the Impact of Constellation Configuration over Multistatic SAR Images', in 'Proceedings - 2021 7th Asia-Pacific Conference on Synthetic Aperture Radar, APSAR 2021' (Institute of Electrical and Electronics Engineers Inc., 2021)

9 Renga, A., Graziano, M.D., Moccia, A.: 'Formation Flying SAR: Analysis of Imaging Performance by Array Theory'*IEEE Trans Aerosp Electron Syst*, 2021, **57**, (3), pp. 1480–1497.

10 Krieger, G., Fiedler, H., Rodriguez-Cassola, M., Hounam, D., Moreira, A.: 'System Concepts for Bi-and Multi-Static SAR Missions', in 'International Radar Symposium (IRS)' (2003)

11 Hagelberg, A., Andre, D., Finnis, M.: 'Non-overlapping trajectory Multistatic SAR Coherent Change Detection', in 'IET International Conference on Radar Systems' (2022)

12 Keydel, W.: 'Present and Future Airborne and Space-borne Systems'*NATO STO*, 2007, pp. 1–28.

13 Krieger, G., Moreira, A.: 'Multistatic SAR satellite formations: Potentials and challenges', in 'International Geoscience and Remote Sensing Symposium (IGARSS)' (2005), pp. 2680–2684

14 Andre, D., Blacknell, D., Morrison, K.: 'Spatially variant incoherence trimming for improved SAR CCD', in 'Algorithms for Synthetic Aperture Radar Imagery XX, Vol 8746' (SPIE Defense, Security and Sensing, 2013), pp. 153–164

15 Doerry, A.W.: 'SAR data collection and processing requirements for high quality coherent change detection', in 'Radar Sensor Technology XII' (SPIE, 2008), p. 694706

16 Airbus: 'https://www.airbus.com/en/newsroom/press-releases/2019-09-airbus-to-develop-technology-for-ultra-high-resolution-satellites'

17 Hawkins, B., Anderson, M., Prager, S., Chung, S.J., Lavalle, M.: 'Experiments with small UAS to support SRA tomographic mission formulation', in 'International Geoscience and Remote Sensing Symposium (IGARSS)' (Institute of Electrical and Electronics Engineers Inc., 2021), pp. 643–646

18 Harmer, S.W., De Novi, G.: 'Distributed Antenna in Drone Swarms: A Feasibility Study'*MDPI Drones*, 2023, **7**, (2).

19 Cloude, S.R.: 'Polarimetric SAR interferometry'*IEEE Transactions on Geoscience and Remote Sensing*, 1998, **36**, (5 PART 1), pp. 1551–1565.

20 Hagelberg, A., Andre, D., Finnis, M.: 'Laboratory multistatic and multipolar SAR CCD investigation', in '5th International Conference on Synthetic Aperture in Sonar and Radar' (Institute of Acoustics, 2023)

21 Cha, M., Phillips, R.D., Wolfe, P.J., Richmond, C.D.: 'Two-Stage Change Detection for Synthetic Aperture Radar'*IEEE Transactions on Geoscience and Remote Sensing*, 2015, **53**, (12), pp. 6547–6560.

22 Bondre, A.S., Richmond, C.D.: 'Theoretical Analysis of a Symmetric Two-Stage Change Detector for SAR Images'*IEEE Transactions on Geoscience and Remote Sensing*, 2022, **60**.

23 Cha, M., Phillips, R.D., Wolfe, P.J.: 'Combined intensity and coherent change detection for synthetic aperture radar', in 'ICASSP, IEEE International Conference on Acoustics, Speech and Signal Processing - Proceedings' (Institute of Electrical and Electronics Engineers Inc., 2014), pp. 8120–8123

24 Doerry, A.W.: 'Collecting and Processing Data for High Quality CCD Images'*Sandia National Laboratories, Report no. SAND2007-1545*, 2007.

25 Lee, S.-K., Kugler, F., Hajnsek, I., Papathanassiou, K.P.: 'The Impact of Temporal Decorrelation over Forest Terrain in Polarimetric SAR Interferometry', in 'Proceedings of the International Workshop on Applications of Polarimetry and Polarimetric Interferometry (Pol-InSAR). ESA' (2009)

26 López-Martínez, C., Pottier, E.: 'Basic Principles of SAR Polarimetry', in 'Remote Sensing and Digital Image Processing' (Springer Science and Business Media B.V., 2021), pp. 1–58

27 Lee, J.S., Grunes, M.R., Ainsworth, T.L., Pottier, E., Krogager, E., Boerner, W.M.: 'Quantitative comparison of classification capability: Fully-polarimetric versus partially polarimetric SAR', in 'International Geoscience and Remote Sensing Symposium (IGARSS)' (IEEE, 2000), pp. 1101–1103

28 Andre, D.: 'Bistatic SAR coherence improvement through spatially variant polarimetry', in 'IMA Conference on Mathematics in Defence' (2015)

29 Crisp, D.J., Stacy, N.J.S., Hudson, D.A., Pincus, P.B., Goh, A.S.: 'Polarimetric Analysis of Maritime SAR Data Collected with the DSTO Ingara X-Band Radar', in 'IEEE International Geoscience and Remote Sensing Symposium' (2007)

30 Cloude, S., Pottier, E.: 'A review of target decomposition theorems in radar polarimetry'*IEEE Transactions on Geoscience and Remote Sensing*, 1996, pp. 498–518.

31 Bombrun, L., Bistatic, L.B.: 'Bistatic Polarimetric SAR Decomposition in Terms of Roll-Invariant Parameters' (2011)

32 Wilks, D.S.: 'Statistical methods in the atmospheric sciences' (Elsevier, 2006, 2nd edn.)

33 Davidovitz, B., Wolfgang-Martin, M.: 'Extension of Kennaugh's Optimal Polarization Concept to the Asymmetric Scattering Matrix Case'*IEEE Trans Antennas Propag*, 1986, **34**, (4).

34 Doswell, C.A., Davies-Jones, R., Keller D. L.: 'On summary measures of skill in rare event forecasting based on contingency tables'*Weather Forecast*, 1990, **5**, pp. 576–585.

35 Roebber, P.J.: 'Visualizing multiple measures of forecast quality'*Weather Forecast*, 2009, **24**, (2), pp. 601–608.

36 National Oceanic and Atmospheric Administration (NOAA), Space Weather Prediction Center: 'Forecast Verification Glossary (https://www.swpc.noaa.gov/content/forecast-verification)'

37 Chicco, D., Jurman, G.: 'The advantages of the Matthews correlation coefficient (MCC) over F1 score and accuracy in binary classification evaluation'*BMC Genomics*, 2020, **21**, (1).

38 Chicco, D., Starovoitov, V., Jurman, G.: 'The Benefits of the Matthews Correlation Coefficient (MCC) over the Diagnostic Odds Ratio (DOR) in Binary Classification Assessment'*IEEE Access*, 2021, **9**, pp. 47112–47124.

39 Chai, T., Draxler, R.R.: 'Root mean square error (RMSE) or mean absolute error (MAE)? -Arguments against avoiding RMSE in the literature'*Geosci Model Dev*, 2014, **7**, (3), pp. 1247–1250.